Eur. Phys. J. B **5**, 859–867 (1998)

THE EUROPEAN PHYSICAL JOURNAL B

Static magneto-optical birefringence of size-sorted $\gamma-Fe_2O_3$ nanoparticles

E. Hasmonay[1], E. Dubois[2], J.-C. Bacri[1,a], R. Perzynski[1,b], Yu.L. Raikher[3], and V.I. Stepanov[3]

[1] Laboratoire des Milieux Désordonnés et Hétérogènes, Université Pierre et Marie Curie, Tour 13, Case 78, 4 place Jussieu, 75252 Paris Cedex 05, France
[2] Laboratoire des Liquides Ioniques et Interfaces Chargées, Université Pierre et Marie Curie, Bâtiment F, Case 63, 4 place Jussieu, 75252 Paris Cedex 05, France
[3] Laboratory of Kinetics of Anisotropic Fluids, Institute of Continuous Media Mechanics, Urals Branch of the Russian Academy of Sciences, 1 Korolyov St., Perm 614013, Russia

Received: 9 January 1998 / Received in final form and Accepted: 5 May 1998

Abstract. Magnetic birefringence experiments under static field are performed on ionic ferrofluid samples based on $\gamma-Fe_2O_3$. A colloidal size-sorting of the particles allows to obtain narrow size distributions. The optical birefringence of the solutions is found positive and can be described by a Langevin formalism. It scales as H^2 in the low field limit. In the high field limit the particles size dependence of the saturation birefringence is compatible with a surface anisotropy constant $K_S = 2.8 \times 10^{-2}$ erg cm^{-2} associated with a particle elongation of 1.25 both coherent with Néel predictions of surface anisotropy in small grains.

PACS. 75.50.Mm Magnetic liquids – 78.20.Ls Magnetooptical effects – 78.66.J Nanocrystalline materials, optical properties

1 Introduction

Chemically synthesized [1] ionic ferrofluids based on maghemite ($\gamma-Fe_2O_3$) nanoparticles exhibit strong optical birefringence under magnetic fields [2]. Isotropic in zero field, the solutions in which the particles are dispersed become optically uniaxial under field. This macroscopic effect, which saturates in high fields, is related to the microscopic optical anisotropy of the particles and to their orientation with respect to the field direction. If they are properly dispersed in their carrier, it is an intrinsic property of the particles: at low volume fraction Φ, the birefringence is then proportional to Φ. Such optical experiments [3] are useful tools to probe the dynamics of the particles carrier, for example their viscoelastic properties [4].

However the sign and the physical origin of this particle optical anisotropy is still under discussions. The birefringence may have several origins:

- *a field-induced effect in the particle material* [5], however, within the accuracy and in the field range of standard measurements, no optical anisotropy of the solutions is observed if the particles are dispersed in a zero magnetic field in a carrier subsequently frozen (for example, a tight polymeric matrix [2] or a silica aero-gel [6]);

- *the internal optical anisotropy of the magnetic particles*, but as tested by X-rays and neutron scattering the ferrite core of the particles has a cubic crystalline structure unable to induce birefringence; a tetragonal order of vacancies exists in bulk $\gamma-Fe_2O_3$, but it disappears in nanosized particles smaller than 200 nm [7];

- *a shape anisotropy of the particles*, electron microscopy [8] evidences more rock-like particles than elongated ellipsoids.

Recently a size sorting of the ferrofluid particles by a colloidal method [9] has allowed a definite progress in the knowledge of the magnetic anisotropy of those small $\gamma-Fe_2O_3$ nanograins. A FerroMagnetic Resonance experiment (FMR) [10] has demonstrated that this anisotropy is positive and uniaxial, coming from surface magnetic defects. It is presumably related to the magnetically disordered surface and to a small shape eccentricity. These points are compatible with a quasielastic neutron scattering experiment [11]. Several other works [12–15] report on the importance of surface effects in the fine grain magnetism at the scale of 2 to 10 nm, in particular for iron oxide materials. We shall investigate here, using a magnetic birefringence experiment, the optical anisotropy of our $\gamma-Fe_2O_3$ nanograins.

In this paper after a short theoretical recall on the magnetic birefringence of a monodisperse ferrofluid solution of monodomain particles, we present our size-sorted samples and the birefringence experiments. The results are

[a] *Also at:* Université Denis Diderot (Paris VII), UFR de Physique, 2 place Jussieu, 75251 Paris Cedex 05.
[b] e-mail: rperz@ccr.jussieu.fr

then compared to different models and discussed in terms of polydispersity and surface anisotropy of the particles.

2 Theoretical background

We assume that all the particles in the suspension are identical with a volume V. From the magnetic viewpoint, each particle is considered in the model as a single-domain with a uniform magnetization m_S and a uniaxial magnetic anisotropy. For the latter, its magnitude is characterized by the energy E_a and its direction by the unit vector $\boldsymbol{\nu}$ along the easy axis of the particle. Given that, the particle magnetic moment may be written as $\boldsymbol{\mu} = \mu\mathbf{e}$ where $\mu = m_S V$ and $||\mathbf{e}|| = 1$. The orientation-dependent part of the magnetic energy of the particle in the external field $\mathbf{H} = H\mathbf{h}$ (where $||\mathbf{h}|| = 1$) then writes

$$U = -\mu H(\mathbf{e}\cdot\mathbf{h}) - E_a(\mathbf{e}\cdot\boldsymbol{\nu})^2. \tag{1}$$

As is shown in references [16–18], the birefringence of a dilute suspension of anisotropic particles is determined by the orientational order tensor

$$\alpha_{ik} = \frac{3}{2}\left(\langle\nu_i\nu_k\rangle - \frac{1}{3}\delta_{ik}\right) \tag{2}$$

where in the static case the statistical average must be taken over the equilibrium distribution

$$W_0 = Z_0^{-1}\exp(-U/k_BT)$$
$$Z_0 = \int \exp(-U/k_BT)d\mathbf{e}d\boldsymbol{\nu} \tag{3}$$

with U from equation (1).

This averaging may be carried out rigorously and yields

$$\alpha_{ik} = \frac{3}{2}\left[1 - \frac{3L(\xi)}{\xi}\right]\left[\frac{d}{d\sigma}\ln R(\sigma) - \frac{1}{3}\right] \times\left(\frac{3}{2}h_ih_k - \frac{1}{2}\delta_{ik}\right), \tag{4}$$

where the dimensionless parameters

$$\xi = m_SVH/k_BT, \quad \sigma = E_a/k_BT \tag{5}$$

are introduced, ξ (the Langevin parameter) and σ being respectively the magnetic energy and the anisotropy energy of one grain normalized to the thermal energy k_BT.

The functions constituting expression (4) are well-known: $L(\xi)$ is the first Langevin function, $L_2(\xi) = 1-3L(\xi)/\xi$ is the second Langevin function and the properties of the integral

$$R(\sigma) = \int_0^1 \exp(\sigma x^2)dx$$

were studied, for example, in reference [19]. The asymptotic forms for the particle-size dependent factors entering expression (4) are:

$$1 - \frac{3L(\xi)}{\xi} = \begin{cases}\xi^2/15 & \text{if } \xi \ll 1,\\ 1-3/\xi & \text{if } \xi \gg 1,\end{cases}$$
$$\frac{3}{2}\left[\frac{d}{d\sigma}\ln R(\sigma) - \frac{1}{3}\right] = \begin{cases}2\sigma/15 & \text{if } \sigma \ll 1,\\ 1-3/2\sigma & \text{if } \sigma \gg 1.\end{cases} \tag{6}$$

Both functions grow monotonously with their respective arguments, and both of them eventually tend to the unity saturation levels.

An important conclusion following from equations (4–6) is that to achieve a high degree of orientation not just a high magnetic field (*i.e.*, $\xi \gg 1$) is necessary. To the same extent a high magnetic anisotropy (*i.e.*, $\sigma \gg 1$) is essential. In other words, providing the particles are magnetically soft ($\sigma \ll 1$), the suspension would dwell in an orientationally disordered state whatever high is the applied field.

Writing the pertinent expressions of references [16–18] in the framework of an effective medium theory for the birefringence Δn, one arrives at a simple formula

$$\Delta n = B\alpha\Phi \tag{7}$$

where α is the component of tensor (4) along the direction of the applied field. In our notations it reads

$$\alpha = \left[1 - \frac{3L(\xi)}{\xi}\right]\left[\frac{d}{d\sigma}\ln R(\sigma) - \frac{1}{3}\right]. \tag{8}$$

The coefficient B may be written as

$$B = \frac{1}{2n_{solv}}(\chi_{\parallel}^{el} - \chi_{\perp}^{el}) \tag{9}$$

n_{solv} being the optical index of the low absorbing carrier and $\chi_{||}^{el}$ (respectively $\chi_{\perp}^{el}$) being the effective electric susceptibility of the particle along (respectively perpendicular) its anisotropy axis. The explicit form of $(\chi_{||}^{el} - \chi_{\perp}^{el})$ depends on the physical origin of the optical anisotropy [16–18].

Thus, for a given value of σ, Δn tends toward a maximum Δn_S in high field which is proportional to the particle volume fraction Φ:

$$\Delta n_S = \delta n_0\Phi \;\text{ with }\; \delta n_0 = B\left[\frac{d}{d\sigma}\ln R(\sigma) - \frac{1}{3}\right] \tag{10}$$

and we may write:

$$\text{for } \xi \ll 1 \quad \Delta n = \Delta n_S\frac{\xi^2}{15} \propto H^2 \tag{11}$$

$$\text{for } \xi \gg 1 \quad \Delta n = \Delta n_S\left(1 - \frac{3}{\xi}\right). \tag{12}$$

3 Ferrofluid samples

Our magnetic liquid samples are ionic ferrofluids, based on nanoparticles made of an iron oxide: maghemite,

$\gamma-Fe_2O_3$. They are chemically synthesized after the Massart's method [1]: a coprecipitation in an alkaline medium of an aqueous mixture of Fe^{2+} and Fe^{3+} salts. Bulk maghemite has an inverse spinel structure with Fe^{3+} ions vacancies in the octahedral metal sublattice. At room temperature, bulk magnetization of $\gamma-Fe_2O_3$ is $m_S = 400$ G, with a Curie temperature extrapolated to 590 °C, well above room temperature. The magnetocrystalline volumic anisotropy of bulk maghemite is cubic [20] with $K_V = 4.7 \times 10^{+4}$ erg cm^{-3}. Our $\gamma-Fe_2O_3$ nanoparticles of typical size 10 nm have:

- a monodomain magnetic core of maghemite, as tested by X-rays and neutron diffraction;
- surrounded by a more disordered spin layer, giving an amorphous foot to the X-rays diffraction pattern and leading to a slight size dependence of m_S (this dependence is here always less than 20% and will be neglected in the present work).

FMR experiments have evidenced [10] the uniaxial magnetic anisotropy of those particles, with an anisotropy constant equal to $K_s = 2.8 \times 10^{-2}$ erg cm^{-2}. This positive anisotropy finds its origin in the poorly crystallized spins layer which is localized at the particle surface and has a thickness of the order of an elementary crystalline cell.

Those chemically synthesized particles are also macroions: they bear surface ligands (here either hydroxoligands (-OH) or citrate ligands (-LH)) leading to a superficial density of charges $|\Sigma| \approx 20$ μCcm^{-2} [8,21] in the appropriate range of pH (in water: pH < 6 or pH > 9 for ligands -OH and $5 <$ pH < 9 for the ligands -LH). If no extra electrolyte is added, the strong electrostatic interparticle repulsions allow the ferrofluid solutions to be colloidally stable even under magnetic fields [22]. The volume fraction Φ of magnetic particles is determined by chemical titration of ions.

The ferrofluid samples present a size distribution of magnetic particles which is, in a first approximation, well described by a log-normal distribution of particles diameters [23]:

$$f(d) = \frac{1}{\sqrt{2\pi}sd} \exp\left[-\frac{\ln^2(d/d_0)}{2s^2}\right] \qquad (13)$$

where $\ln d_0$ corresponds to the mean value of $\ln d$ and s is the standard deviation. This size distribution may be probed by various techniques [8,23–25]:

- the geometric size by electron microscopy or (non polarized) Small Angle Neutron Scattering (SANS);
- the crystalline size by Debye-Scherrer X-rays determination;
- the magnetic size by magnetization measurements or polarized SANS.

All these determinations are found close to each other with our $\gamma-Fe_2O_3$ samples [8,25]. After the chemical synthesis, the ferrofluid samples are rather polydisperse with a value ranging from 0.3 to 0.5. The addition of an electrolyte to the ferrofluid solution may destabilize the colloid. It leads to a phase separation in two liquid phases of different concentrations [26], the biggest particles going preferably to the dense phase. As the phase diagram of the colloidal demixion is size dependent, it is possible by a fractionated precipitation to separate the initial sample in several ones of different mean sizes [9,26]. These new samples are stable colloids without added salts [8,21,27] and have a standard deviation s lowered down to 0.15–0.25.

Table 1. This table presents for each sample, its ligand and its liquid carrier, the diameter d_0^{magn} and standard deviation s^{magn}, obtained by the magnetization characterization (fit of the experimental magnetization curve by the first Langevin function associated to the log-normal distribution function). It also gives the diameter d_{RX} from X-rays measurements when available and the parameter σ^{magn} calculated for each sample (see text for its expression).

Sample	Surface ligands	Carrier liquid	d_0^{magn} (nm)	s^{magn}	d_{RX} (nm)	σ^{magn}
A	-OH	water	13	0.4	-	3.6
B	-OH	water	11	0.4	-	2.6
C	-LH	glycerine	6.6	0.4	-	0.9
D	-OH	water	8.5	0.3	10	1.5
E	-OH	water	9	0.3	-	1.4
F	-OH	water	7	0.3	10.4	0.9
G	-OH	water	-	-	10.4	-
H	-LH	glycerine	6.8	0.2	-	0.9
I	-LH	glycerine	8.2	0.15	-	1.4
J	-LH	glycerine	6.9	0.15	-	1

In this work, we compare samples of various d_0 with standard deviation s ranging from 0.15 to 0.4. In order to avoid interparticle interactions the volume fraction Φ of particles is always less than 1.5% and the ionic strength as low as possible. The liquid carrier is either water or glycerine, at room temperature. The colloidal stability of the samples is checked by an optical diffraction method up to a magnetic field of 1 T. Magnetic size characteristics of the samples are presented in Table 1, they are deduced from magnetization measurements (and for some few samples from Debye-Scherrer X-rays determination). Because of the rotational degree of freedom of the particles, liquid ferrofluid solutions are superparamagnetic materials. In the dilute limit ($\Phi \ll 1$), the magnetization curve $M(H)$ is ruled by the Langevin formalism and is a superposition of single-grains contributions [2]. Neglecting the small size dependence of m_S, the magnetic size distribution is then deduced from a best fit of the reduced magnetization curve to $M/M_{sat} = \int d^3L(\xi)f(d)dd/\int d^3f(d)dd$, the saturation value M_{sat} of M being approximated by the maximum value of M at 1 T. The Debye-Scherrer measured diameter averages the size distribution as $d_{RX} = d_0 \exp(2.5s^2)$ [28].

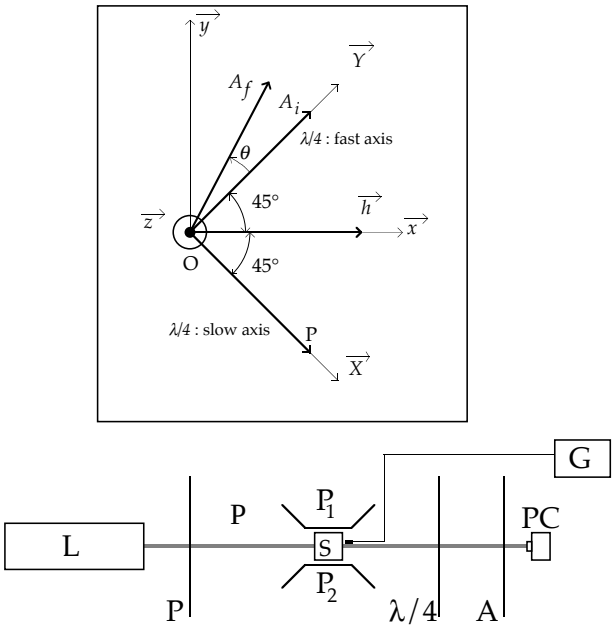

Fig. 1. First experimental optical device. Laser (L) beam goes through polarizer (P), sample (S) submitted to a constant magnetic field (created by polar pieces (P1, P2) measured by the Hall effect probe linked to a gaussmeter (G)), a quarter wave plate ($\lambda/4$), an analyzer (A). Transmitted light intensity is detected by a photocell (PC). The inset presents respective directions of polarizer (P) parallel to slow axis of quarter wave plate (**X**), constant magnetic field (**H**), initial direction of analyzer (A_i) perpendicular to (P) and parallel to the fast axis of quarter wave plate (**Y**) and final direction of analyzer (A_f) which makes an angle θ with (A_i).

Table 1 presents the samples characteristics, their surface ligands, liquid carrier and size distribution. An evaluation of the parameter $\sigma^{magn} = E_a/k_BT = K_S\pi(d_0^{magn})^2/k_BT$ is given for each sample. We perform experiments in the range $\sigma^{magn} \geq 1$.

4 Optical experiments

4.1 Determination of the birefringence sign with a simple optical device

The sign of the magnetic birefringence of a ferrofluid is here determined with the optical device of Figure 1: we analyze the polarization of the light transmitted by the ferrofluid sample under field. The He-Ne laser light (L) of wavelength $\lambda_0 = 632.8$ nm propagates along (O**z**), goes through a polarizer (P), the ferrofluid sample (S) submitted to an horizontal magnetic field produced by the polar pieces (P1, P2) of an electromagnet, a quarterwave plate ($\lambda/4$) (for the wavelength of the laser) and an optical detector (PC). The angle of the optical rotating elements are recorded with a precision of 0.5 degree. Crossed polarizer (P) and analyzer (A_i) are first put at 45° of the horizontal magnetic field $\mathbf{H} = H\mathbf{h}$ (see inset of Fig. 1). The $\lambda/4$ plate is then introduced with its slow optical axis parallel to the polarizer (P) (its fast axis is thus parallel to (A_i)).

The ferrofluid sample is set in a non-birefringent glass cell of thickness e and the magnetic field H is switched on. H varies from 0 to 4000 Oe by 500 Oe steps. The glass cell is thermally connected to a Peltier device to control the sample temperature. As magnetic field is switched on, the particles align along the field, and the solution becomes optically birefringent with an optical axis collinear to the applied magnetic field. The medium then behaves as a birefringent plate characterized by a phase-lag φ related to the birefringence Δn of the sample of thickness e by $\varphi = 2\pi e\Delta n/\lambda_0$ (Δn is defined by $\Delta n = n_{||} - n_\perp$, $n_{||}$ being the optical index in the direction of the magnetic field and $n_\perp$ the optical index in the perpendicular direction). Our ferrofluid solutions are also dichroic. In a first approximation we neglect this effect which is small. We shall go back to this point with the second optical measurement.

At the output of (P) the wave is linearly polarized and the electric field writes in the referential (O, **x**, **y**) (see inset of Fig. 1) :

$$\mathbf{E}_P \left(\frac{E_{laser}}{\sqrt{2}} \cos\omega t, -\frac{E_{laser}}{\sqrt{2}} \cos\omega t \right). \qquad (14)$$

After crossing the ferrofluid cell of transmission coefficient t it gets an elliptic polarization. In a first approximation t is taken isotropic and independent of the direction of the applied magnetic field **H**. Under **H** the components of the electric field become:

$$\mathbf{E}_{FF} \left(\frac{E_{laser}}{\sqrt{2}} t \cos(\omega t - \varphi), -\frac{E_{laser}}{\sqrt{2}} t \cos\omega t \right). \qquad (15)$$

and projected along (O, **X**, **Y**) at 45° of the magnetic field direction:

$$\mathbf{E}_{FF} \left(E_{laser} t \cos\frac{\varphi}{2} \cos\left(\omega t - \frac{\varphi}{2}\right), \right.$$
$$\left. E_{laser} t \sin\frac{\varphi}{2} \sin\left(\omega t - \frac{\varphi}{2}\right) \right). \qquad (16)$$

Going through the $\lambda/4$ plate, the component E_X gets a $\pi/2$ delay and the wave is again linearly polarized.

The components E_X and E_Y have then the same phase

$$\mathbf{E}_{\lambda/4} \begin{vmatrix} E_X = E_{laser} t \cos\frac{\varphi}{2} \cos\left(\omega t - \frac{\varphi}{2} - \frac{\pi}{2}\right) \\ \quad = E_{laser} t \cos\frac{\varphi}{2} \sin\left(\omega t - \frac{\varphi}{2}\right) \\ E_Y = E_{laser} t \sin\frac{\varphi}{2} \sin\left(\omega t - \frac{\varphi}{2}\right) \end{vmatrix} . \qquad (17)$$

The direction of the linear polarization forms an angle $\varphi/2$ with **Y**, $\tan(\varphi/2) = E_Y/E_X$; there is some light transmitted by the device. Turning the analyzer from its first position A_i (perpendicular to the polarizer), to the position A_f, by extinguishing the transmitted light gives both the sign of φ and its value $\varphi = 2\theta$. The sign of φ is given by the sign of θ in the plane (O, **x**, **y**).

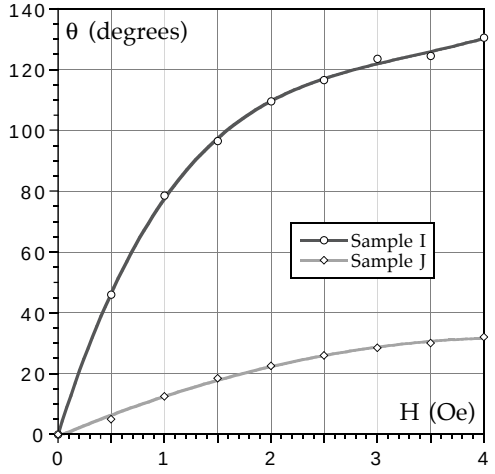

Fig. 2. Measured angle θ as a function of applied magnetic field H as determined with the optical device of Figure 1. (○) sample I; $\Phi = 1.5\%$; $e = 700$ μm, (◊) sample J; $\Phi = 1.5\%$; $e = 500$ μm. The full lines are guides for the eyes.

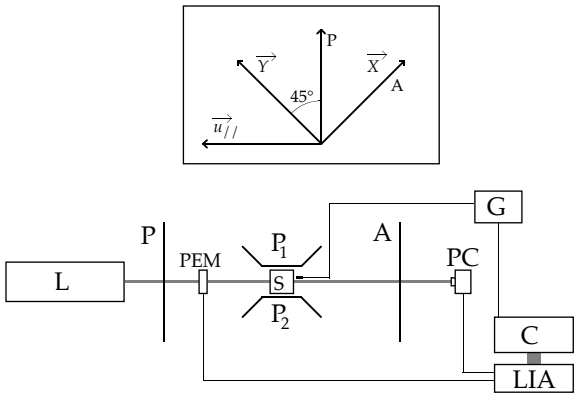

Fig. 3. Second optical device. Laser (L) beam goes through polarizer (P), PhotoElastic Modulator (PEM), sample (S) put between polar pieces (P1, P2), analyzer (A) and photocell (PC). The field is measured with a Hall effect probe connected to a gaussmeter (G). The PhotoElastic Modulator oscillation frequency is used as a reference by the Lock-In Amplifier (LIA) to detect the ω component of the light intensity transmitted by the setup. Gaussmeter and lock-in amplifier are connected to a computer (C) which stores the experimental data. The inset displays relative orientations of optical elements: analyzer (A), polarizer (P), constant magnetic field ($\mathbf{H} = \mathbf{u}_{\|}$) and photoelastic modulator ($\mathbf{X}$ and $\mathbf{Y}$).

Figure 2 presents the results $\Delta n = \theta\lambda_0/\pi e$ as a function of the applied field H obtained with sample I (cell thickness $e = 700$ μm) and sample J ($e = 500$ μm). The birefringence is found positive and is an increasing function of the magnetic field H.

4.2 Optical device with an optical modulator: experimental determination of Δn(H)

The optical device used here is shown in Figure 3. The sample (S) of thickness e is put between the pole pieces (P_1, P_2) of an electromagnet ($H_{max} \approx 1.1 \times 10^4$ Oe), in the beam of a He-Ne laser (L) of low power (1 mW) between a polarizer (P) and an analyzer (A). The photocell (PC) detects the transmitted light. A PhotoElastic Modulator (PEM) is interposed between the polarizer and the ferrofluid sample. The PEM modulates at 50 kHz the phase of the signal between two perpendicular directions. A Lock-In amplifier (LIA) compares the electric signal from the photocell (PC) to the reference signal from the modulator, and give the component at the same frequency.

The optical set-up with axes of magnetic field $\mathbf{H}$ ($\mathbf{h} = \mathbf{u}_{||}$), polarizer P ($= \mathbf{u}_{\perp}$), analyzer A and photoelastic modulator ($\mathbf{X}, \mathbf{Y}$) is sketched in the inset of Figure 3. The electric field $\mathbf{E}$ at the output of the modulator is:

$$\mathbf{E} = (E_0/\sqrt{2})(\mathbf{X} + \mathbf{Y}e^{i\delta}) \tag{18}$$

with $\delta = a\sin(\omega t)$ and $\omega/2\pi = 50$ kHz. After crossing the sample, the electric field is then:

$$\mathbf{E} = (E_0/\sqrt{2})\left(\sqrt{t_{\|}}(e^{i\delta} - 1)\mathbf{u}_{\|} + \sqrt{t_{\perp}}(e^{i\delta} + 1)e^{i\varphi}\mathbf{u}_{\perp}\right) \tag{19}$$

with $\varphi = 2\pi\Delta ne/\lambda$ and $t_{||}$ and $t_{\perp}$ transmission coefficients (now taken respectively parallel to field and perpendicular) defined in intensity.

At the analyzer output the electric field becomes:

$$\mathbf{E}_2 = \left(E_0/2\sqrt{2}\right)\left(\sqrt{t_{||}}\left(1 - e^{i\delta}\right) + \sqrt{t_{\perp}}\left(e^{i\delta} + 1\right)e^{i\varphi}\right)\mathbf{X}. \tag{20}$$

The light intensity I collected by the photocell is:

$$I = \left(E_0^2/4\right)\left[t_{||}\left(1 - \cos\delta\right) + t_{\perp}\left(1 + \cos\delta\right) - 2\sqrt{t_{||}t_{\perp}}\sin\varphi\sin\delta\right]. \tag{21}$$

Expanding and in terms of Bessel functions:

$$I = \left(E_0^2/4\right) \times \left\{ \begin{array}{l} \left[\left(t_{||} + t_{\perp}\right) + \left(t_{\perp} - t_{||}\right)J_0(a)\right] \\ -4\sqrt{t_{||}t_{\perp}}J_1(a)\sin\varphi\sin\omega t \\ +2\left(t_{\perp} - t_{||}\right)J_2(a)\cos 2\omega t \end{array} \right\}. \tag{22}$$

Thus intensity component I_2 at pulsation 2ω is proportional to the sample dichroism whereas the intensity component I_1 at pulsation ω is related to the sample birefringence. For a modulation $a = \pi/2$, $J_1(a) = 0.56$ is close to its maximum and the I_1 component is optimized. For our ferrofluids I_1 is proportional to $\sin\varphi$. If e is well chosen several oscillations occur in our range of field (see Fig. 4). The variations of Δn as a function of the magnetic field may be deduced from these measurements. Figure 5 presents the results for sample I when increasing the magnetic field in a log-log plot representation (Δn values are found identical for increasing or decreasing the magnetic field). In the Φ range of the experiment and within its 5% accuracy, Δn is proportional to the volume fraction Φ

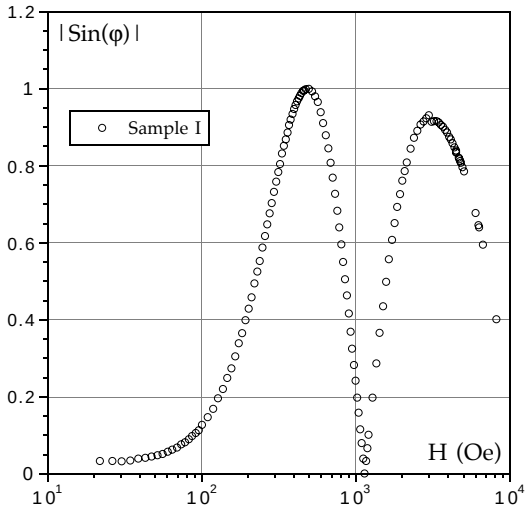

Fig. 4. Intensity component I_1 as a function of applied magnetic field H as determined with the device of Figure 3. For sample I; $\Phi = 1.5\%$; $e = 700$ μm. I_1 is proportional to $|\sin\varphi|$.

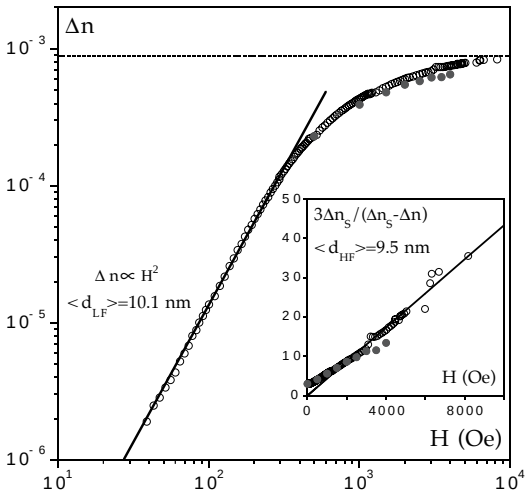

Fig. 5. Birefringence Δn of sample I ($\Phi = 1.5\%$) as a function of applied magnetic field H in a log-log representation. Open (respectively gray) symbols: Δn determined with the optical device of Figure 3 (resp. Fig. 1). The dotted horizontal line marks the maximum $\Delta n_S = 8.8 \times 10^{-4}$ of Δn. The full line is a best fit of the low field behavior: $\Delta n \propto H^2$. The inset illustrates the high field behavior of Δn. For d_{LF} and d_{HF} definitions, see the text.

of particles. These both facts strongly indicate that in such solutions magnetic birefringence is not due to a cooperative process of particle agglomeration in the field but to a single particle effect. No influence of the liquid carrier, water or glycerine is detected in our experiment. For a comparison, the Δn variations of sample I obtained by the first experimental technique (see Sect. 4.1) are also plotted in Figure 5.

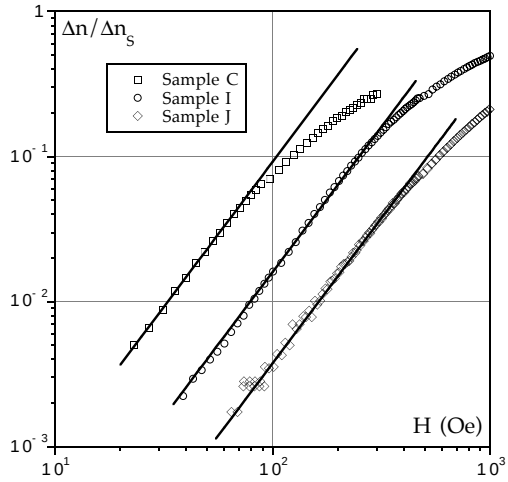

Fig. 6. Reduced birefringence $\Delta n/\Delta n_S$ as a function of applied magnetic field H in a log-log representation for three different samples – full lines are best fits of the low field behavior $\Delta n \propto H^2$. They respectively correspond to $d_{LF} = 13.4$ nm, $d_{LF} = 10.1$ nm and $d_{LF} = 7.6$ nm for samples C, I and J.

Table 2. This table presents the results of the birefringence experiments d_0^{bir}, s^{bir}, δn_0 and σ^{bir} obtained for by a fit of the experimental curve by the second Langevin function associated to the log-normal distribution function.

Sample	Surface ligands	Carrier liquid	d_0^{bir} (nm)	s^{bir}	δn_0	σ^{bir}
A	-OH	water	19.9	0.4	0.2	8.4
B	-OH	water	14.7	0.4	0.15	4.6
C	-LH	glycerine	7.5	0.4	0.076	1.2
D	-OH	water	10.5	0.3	0.115	2.3
E	-OH	water	9.5	0.3	0.093	1.9
F	-OH	water	8.4	0.3	0.08	1.5
G	-OH	water	12.8	0.2	0.13	3.5
H	-LH	glycerine	6.6	0.2	0.044	0.9
I	-LH	glycerine	9.2	0.15	0.058	1.8
J	-LH	glycerine	6.1	0.2	0.037	0.8

5 Discussion

5.1 Comparison to the monodisperse model

5.1.1 Low field behavior

Our samples exhibit in low magnetic fields a behavior compatible with the expression (10) of the monodisperse model of Section 2. In low fields Δn is found to be proportional to H^2 (see Figs. 5 and 6). This H^2 behavior is a second point demonstrating that the birefringence of the samples is coming from individual particles at least in low fields. From expression (11), a magnetic size of the particles may be deduced. For example for sample I of Figure 5 we find a low-field-averaged particle diameter d_{LF} of 10.1 nm close to the magnetic characteristics of the particles.

5.1.2 High field behavior

The birefringence $\Delta n(H)$ always saturates in high fields to a value Δn_S proportional to Φ. The ratio $\delta n_0 = \Delta n_S/\Phi$ is independent of Φ but depends on the sample (see Tab. 2). For example for sample I: $\delta n_0 = 5.8 \times 10^{-2}$; in Table 2 δn_0 ranges from 0.04 to 0.2. Such a particle size dependence is compatible with expression (10).

The experimental evolution of $\Delta n(H)$ toward saturation Δn_S is compared, for sample I, in the inset of Figure 5, to expression (12): the high field prediction of the monodisperse model. This plot allows another particle size determination. We find for sample I a high-field-averaged particle diameter d_{HF} of 9.5 nm close to the low field one. This is compatible with the small width of the magnetic distribution of this sample.

5.1.3 Polydispersity of the system

Whatever close are d_{LF} and d_{HF}, they are however different. To go on with a comparison to theories, it is now necessary to introduce in the model the polydispersity. However the problem in its full generality is difficult to handle and we have chosen to analyze two extreme situations.

(i) δn_0 is a function of the particle diameter (see Eq. (10) and Tab. 2). In a first analysis we neglect the δn_0 variations for the particles of a given sample along the width of its distribution: we approximate the particles by spheres with a log-normal distribution of diameter and analyze the field variations of Δn to deduce a diameter distribution.

(ii) In a second analysis, we consider only the high field results for which Δn is assimilated to Δn_S. We then approximate the particles by ellipsoids of free eccentricity in order to check the dependencies of δn_0. It opens a discussion on the origin of the optical anisotropy of our ferrofluid solutions and on the possibility of chaining of the particles in very high fields.

5.2 Log-normal distribution of spherical particles

In this first (and standard) approximation, δn_0 is supposed to be weakly dependent on the particle size. We thus neglect its variation among the size distribution of each sample and assimilate here $\delta n_0 = \Delta n_S/\Phi$ to a constant for each sample. We approximate the particles to spheres with a log-normal distribution of diameters (see Eq. (13)) characterized by d_0^{bir} and s^{bir}.

We may then compute:

$$\frac{\Delta n_{LN}(H)}{\Delta n_S} = \frac{\displaystyle\int_0^{+\infty} d^3 \left(1 - \frac{3L(\xi(d,H))}{\xi(d,H)}\right) f(d, d_0^{bir}, s^{bir}) dd}{\displaystyle\int_0^{+\infty} d^3 f(d, d_0^{bir}, s^{bir}) dd}. \quad (23)$$

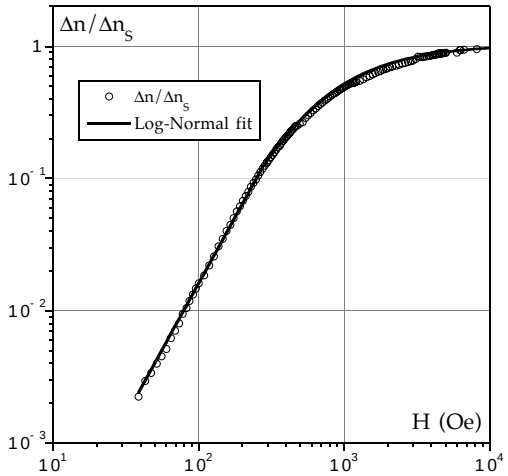

Fig. 7. Reduced birefringence $\Delta n/\Delta n_S$ as a function of applied magnetic field H in a log-log representation for sample I. The full line is the best fit of expression (23) with a log-normal distribution of diameters with $d_0^{bir} = 9.2$ nm and $s^{bir} = 0.15$.

The curve $\Delta n(H)/\Delta n_S$ reduces to a function of two parameters d_0^{bir} and s^{bir} (if m_S is known). Taking d_0^{bir} and s^{bir} as free parameters, a best fit [29] of the experimental measurements $\Delta n(H)/\Delta n_S$ to the expression (23) is plotted for sample I in Figure 7. It leads to $d_0^{bir} = 9.2$ nm and $s^{bir} = 0.15$ compatible with the previous low-field and high-field-averaged diameters namely:

$$d_{LF} = \sqrt[6]{\langle d^9\rangle / \langle d^3\rangle} = d_0^{bir} \exp(6 s^{bir^2}) = 10.5 \text{ nm},$$
$$d_{HF} = \sqrt[3]{\langle d^3\rangle} = d_0^{bir} \exp(1.5 s^{bir^2}) = 9.5 \text{ nm},$$

Table 2 collects d_0^{bir} and s^{bir} for all our samples. The standard deviation s^{bir} and d_0^{bir} are always close to those found from magnetization measurements. However d_0^{bir} is mostly slightly larger than d_0^{magn}.

5.3 Analysis of the high-field results in the hypothesis of elongated ellipsoids

In order to check the limits of the previous description, we now approximate in high fields the solution by an assembly of ellipsoids of eccentricity $\varepsilon = \sqrt{1-(b/a)^2}$ where a/b is the aspect ratio of the ellipsoid. We suppose here the optical anisotropy as coming from the elongated shape of the spheroids, the birefringence being positive.

Then equation (9) reads:

$$B = \frac{1}{2} n_{solv} (N_\perp - N_\parallel) \mathrm{Re}\left[\frac{Q^2}{(1+QN_\perp)(1+QN_\parallel)}\right]. \quad (24)$$

The coefficients $N_\parallel$ and $N_\perp$ in equation (24) are the components (at the frequency of the light) of the depolarization tensor along and perpendicular to the major particle axis, respectively. Note that here the depolarization tensor is normalized as to have a unit trace: $2N_\perp + N_\parallel = 1$. The factor Q in formula (24) is

$$Q = n_{part}^2/n_{solv}^2 - 1 \quad (25)$$

where n_{part} is the refraction index of the particle substance. In this simple model we assume that n_{part} is scalar, although this quantity is complex. The particle material is absorbing as well as refractive, here we have after reference [30], $n_{part} = 3.2 - 0.15i$.

To relate the coefficient B to the particle aspect ratio, we note that for an ellipsoid of revolution:

$$N_\perp = (1 - N_\parallel)/2, \quad N_\perp - N_\parallel = (1 - 3N_\parallel)/2. \tag{26}$$

The analytical expression for $N_\parallel$ in the case of an elongated spheroid reads [31]:

$$N_\parallel = \frac{1-\varepsilon^2}{\varepsilon^2}\left(\frac{1}{2}\ln\frac{1+\varepsilon}{1-\varepsilon} - \varepsilon\right). \tag{27}$$

To simplify the description we make the approximation of a given polydispersity in size for the spheroids but not in aspect ratio letting thus the B parameter to be particle size independent. Assuming that the aspect ratio is not too large, we are allowed to keep the previous spherical approximation for the particle size distribution using the log-normal distribution function of expression (13). We then obtain for the reduced birefringence in high fields:

$$\delta n_0 = \frac{\Delta n_S}{\Phi} = \frac{B\int d^3\left[1 - \dfrac{3L(\xi_M)}{\xi_M}\right]\left[\dfrac{d}{d\sigma}\ln\sigma - \dfrac{1}{3}\right] f(d, d_0^{bir}, s^{bir})dd}{\int d^3 f(d, d_0^{bir}, s^{bir})dd} \tag{28}$$

with $\xi_M = (d/d_M)^3$, $d_M = 2.7$ nm being a "magnetic effective length" at 1 T ($d_M = \sqrt[3]{6k_BT/\pi m_S H}$). The expression (28) depends on the coefficient B, on the size distribution characterized by d_0^{bir} and s^{bir} and on the size dependence of the magnetic anisotropy σ. In our ionic maghemite, σ^{magn} is known [10] to scale as d^2, being dominated by surface contributions. We thus write the current dimensionless value σ as:

$$\sigma = K_S S/k_BT = \pi K_S d^2/k_BT = d^2/d_a^2, \tag{29}$$

where the auxiliary parameter $d_a = \sqrt{k_BT/\pi K_S}$ is an anisotropy effective length. We perform the fitting using the Levenberg-Marquardt method [29]. For the criterion of the quality of the fit we take the specific residual χ^2, that is the total residual divided by the number of experimental points involved in the particular calculation. We perform the attempt of fitting with two "degrees of freedom" *viz.* the anisotropy diameter d_a and the amplitude B, using d_0 and s values from Table 2. The calculation yields the following results:

$$d_a = 6.78 \text{ nm}; \ B = 0.207; \ \chi^2 = 8.70 \times 10^{-5}. \tag{30}$$

An adequate graphic representation of the undertaken fitting should be expressed as a 3D diagram of δn_0 *versus* d_0 and s. Figure 8 shows four cross-sections of this 3D plot for different values of the distribution width s^{bir}. The theoretical curves are calculated with the aid of equations (29, 30).

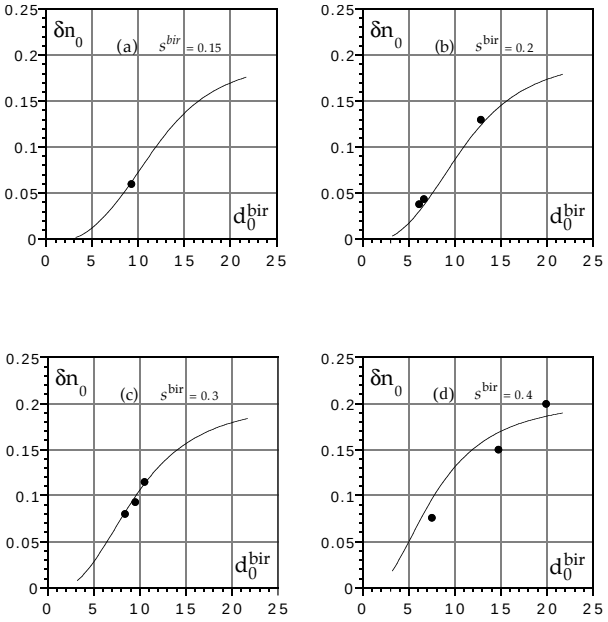

Fig. 8. Results of fitting using the polydisperse model. Each curve corresponds to a particular value of the distribution width s^{bir}. The black dots represent the experimental values of δn_0.

Using relation (29), one gets a determination of the anisotropy constant $K_S = k_BT/\pi d_a^2 = 2.8 \times 10^{-2}$ erg cm^{-2} agreeing rather well with the independent estimation obtained in reference [10] from the high-frequency magnetic measurements (FMR), *i.e.*, by a completely different way of estimation. We have given in Table 2, the dimensionless parameter $\sigma^{bir} = \pi K_S (d_0^{bir})^2/k_BT$ deduced for each sample from these birefringence measurements. For the less polydisperse samples, they are rather close to the magnetic parameter σ^{magn} of Table 1 indicating that the optical anisotropy can be correlated to the magnetic one.

Néel [32] has proposed for magnetic particles with typical size lower than 10 nm, the existence of a structural anisotropy coming from the discontinuity of magnetic interactions between individual spins which reside at the particle surface. This layer is characterized by a surface anisotropy constant K_{SR} and an axis locally perpendicular to the surface. In the case of spherical particles the total contribution of this surface effect is equal to zero but for non-spherical particles (ellipsoids) there is a non-zero contribution. Néel has calculated that the surface layer may be described by the K_S parameter, effective surface anisotropy constant linked to K_{SR} through:

$$K_S = \frac{4}{15}\varepsilon^2 K_{SR}, \tag{31}$$

where ε is the eccentricity of the ellipsoid of revolution and where the value of K_{SR} ranges from 0.1 to 1 erg cm^{-2}.

The effective value of the aspect ratio (a/b) of the particles is a sensitive point. It may be deduced from our fit, through coefficient B and a graphic resolution of equations (24, 25) using the experimental optical index n_{part}. We obtain with our model $a/b = 1.25$ meaning $\varepsilon = 0.6$. It demonstrates the very low degree of aggregation of the particles even under a 1 T magnetic field. Rather in favor of a single particle regime than a developed aggregation, this value is also low enough to justify the use of a spherical approximation in our model for the particle size distribution. Our experimental value of ε put in the formula (31) leads to an evaluation of $K_{SR} = 0.29$ erg cm^{-2} in good agreement with the Néels predictions given above.

6 Conclusion

This work is an experimental investigation of magneto-optical birefringence of ionic ferrofluids based on chemically synthesized $\gamma-Fe_2O_3$ nanoparticles. From this static study on a large number of samples with various particle size distributions, we find that:

- The birefringence Δn of the solution is for our samples and in the low concentration range investigated here, related to a single grain behavior.

- The birefringence of the solution and that of the individual particles are positive. This is compatible with the positive magnetic anisotropy found by FMR measurements on the same samples.

- The magnetic field dependence of Δn can be scaled with a Langevin formalism from the very low field regime (where $\Delta n \propto H^2$) to the very high field regime (where $\Delta n/\Phi$ is a constant dependent on the particle size distribution).

- The origin of the particles optical anisotropy can be correlated to a surface magnetic anisotropy of effective constant $K_S = 2.8 \times 10^{-2}$ erg cm^{-2} and a slight ellipticity of the particles of the order of 1.25 (that could be related to the rock-like shape of the particles). This is a new optical evidence of the importance of the surface magnetism in iron oxide nanodispersions supported by several recent magnetic measurements [10–15].

We thank J. Servais and P. Lepert for their technical assistance. This work was supported by "Le Réseau Formation-Recherche" n° 96P0079 of MENESRIP and from the Russian side by the grant n° 98-02-16453 of Russian Foundation of Basic Research.

References

1. R. Massart, IEEE Trans. Magn. **17**, 1247 (1981).
2. *Magnetic Fluids and Applications Handbook*, edited by B. Berkovski (Begell House Inc. Publ., New-York, 1996).
3. H.W. Davies, J.P. Llewellyn, J. Phys. D **12**, 311 (1979).
4. J.-C. Bacri, D. Gorse, J. Phys. France **44**, 985 (1983); J.-C. Bacri, R. Perzynski, *Complex Fluids*, edited by L. Garrido (Springer-Verlag, Berlin, 1993), p. 85.
5. J. Ferré, G.A. Gehring, Rep. Prog. Phys. **47**, 513 (1984).
6. F. Chaput, J.-P. Boilot, M. Canva, A. Brun, R. Perzynski, D. Zins, J. Non-Cryst. Solids **160**, 177 (1993).
7. K. Haneda, A.H. Morish, Solid State Commun. **22**, 779 (1977); B. Gillot, F. Bouton, J. Solid State Chem. **32**, 303 (1980); L.Q. Amaral, F.A. Tourinho, Braz. J. Phys. **25**, 142 (1995).
8. E. Dubois, Ph.D. thesis, Université Pierre et Marie Curie, Paris (1997).
9. R. Massart, E. Dubois, V. Cabuil, E. Hasmonay, J. Magn. Magn. Mater. **149**, 1 (1995).
10. F. Gazeau, E. Dubois, J.-C. Bacri, F. Gendron, R. Perzynski, Yu.L. Raikher, V.I. Stepanov, *Proceedings of the Second International Workshop on Fine Particle Magnetism* (Bangor, UK, 1996), p. 66; F. Gazeau, J.-C. Bacri, F. Gendron, R. Perzynski, Yu.L. Raikher, V.I. Stepanov, E. Dubois, J. Magn. Magn. Mater. **186**, 175 (1998).
11. F. Gazeau, E. Dubois, M. Hennion, R. Perzynski, Yu.L. Raikher, Europhys. Lett. **40**, 575 (1997).
12. R.H. Kodama, A.E. Berkowitz, E.J. McNiff Jr., S. Foner, Phys. Rev. Lett. **77**, 394 (1996).
13. R.H. Kodama, A.E. Berkowitz, E.J. McNiff Jr., S. Foner, J. Appl. Phys. **81**, 5552 (1997).
14. J.L. Dormann, F. D'Orazio, E. Tronc, P. Prené, J.-P. Jolivet, D. Fiorani, R. Cherkaoui, M. Nogues, Phys. Rev. B **53**, 14291 (1996).
15. C. Bellouard, M. Hennion, I. Mirebeau, J. Magn. Magn. Mater. **140**, 357 (1995).
16. A. Peterlin, H.A. Stuart, Z. Phys. **112**, 129 (1939).
17. Yu.N. Skibin, V.V. Chekanov, Yu.L. Raikher, Sov. Phys. JETP **45**, 496 (1977).
18. P.C. Scholten, IEEE Trans. Magn. **16**, 221 (1980).
19. Yu.L. Raikher, M.I. Shliomis, Adv. Chem. Phys. **87**, 595 (1994).
20. J.B. Birks, Proc. Phys. Soc. B **63**, 65 (1950).
21. E. Dubois, V. Cabuil, J.-C. Bacri, R. Perzynski (to be published).
22. J.-C. Bacri, R. Perzynski, D. Salin, V. Cabuil, R. Massart, J. Magn. Magn. Mater. **85**, 27 (1990).
23. J.-C. Bacri, R. Perzynski, D. Salin, V. Cabuil, R. Massart, J. Magn. Magn. Mater. **62**, 36 (1986).
24. J.-C. Bacri, F. Boué, V. Cabuil, R. Perzynski, Coll. Surf. A **80**, 11 (1993).
25. F. Gazeau, Ph.D. thesis, Université Denis Diderot, Paris, 1997.
26. J.-C. Bacri, R. Perzynski, D. Salin, V. Cabuil, R. Massart, J. Coll. Interf. Sci. **132**, 43 (1989).
27. E. Dubois, V. Cabuil, F. Boué, J.-C. Bacri, R. Perzynski, Progr. Coll. Polym. Sci. **104**, 173 (1997).
28. E. Tronc, D. Bonnin, J. Phys. Lett. **46**, L437 (1985).
29. W.H. Press, B.P. Flannery, S.A. Teukolsky, W.T. Vetterling, *Numerical Recipes, The Art of Scientific Computing* (Cambridge University Press, Cambridge, 1989).
30. J. Lenglet, Ph.D. thesis, Université Denis Diderot, Paris, 1996.
31. L.D. Landau, E.M. Lifshitz, *Electrodynamics of Continuous Media* (Pergamon Press, Oxford, 1960), p. 42.
32. L. Néel, J. Phys. Radium **15**, 225 (1954).